AMD-Vol. 117, Recent Advances in Mechanics
of Structured Continua
ASME 1991

REDIRECTION OF DYNAMIC COMPRESSIVE WAVES IN MATERIALS WITH NEARLY ORTHOGONAL AND RANDOM JOINT SETS*

O. R. Walton, D. M. Maddix, T. R. Butkovich, and F. E. Heuzé
Lawrence Livermore National Laboratory
Livermore, California

ABSTRACT

Two-dimensional discrete-particle (*i.e.*, distinct-element) calculations demonstrate the redirection of particle velocity vectors emanating from a rapidly loaded region such as an explosively loaded borehole or tunnel. Previous simulations have demonstrated redirection of particle motions in randomly fractured media when significant shearing displacements result in dilatancy. This work shows redirection in media with nearly regular and nearly orthogonal joint sets, resulting in asymmetric radiation patterns, even for situations with quite small displacements. Random joint sets (simulated with Voronoi polygons) on the other hand, do not exhibit significant redirection of emanating signals unless significant shear displacements occur. Such redirection could account for anisotropic seismic radiation patterns observed around deeply buried explosions in hard rock. Variation of contact parameters and joint models in these simulations serves to demonstrate that the joint pattern and block kinematics are the dominant mechanisms contributing to this redirection of the compressive waves.

INTRODUCTION

The character of seismic waves emanating from contained underground explosions in fractured or jointed rock may be strongly affected by the discrete nature of the joint patterns pre-existing in the region. It is well known that loads applied to anisotropic media can result in stress fields that align with the principal directions of the anisotropy. Laboratory studies with photoelastic particles have shown that in blocky materials, such as rocks, load transmission is also strongly affected by rotational effects.[1] Not so well known, but recently hypothesized, is the notion that these rotational effects also cause a strong shear induced dilatancy in close packed jointed media. This dilatancy resulting from substantial shear displacements can result in redirection of particle velocities towards directions perpendicular to the shearing.[2] In cratering blasts these shear induced dilatant forces can act as *secondary* seismic sources, emanating from the shear zone as material starts to lift, and can act to significantly alter the direction of the throwout debris.[3]

*Work performed under the auspices of the U.S. Department of Energy by the Lawrence Livermore National Laboratory W-7405-Eng-48

Rock blasting experience has shown that identical charges in different location in hard rock or emplaced in different geometries can result in seismic waves that vary in intensity by factors as large as five.[4] Such variation is partially explained by the proximity and orientation of nearby free surfaces; however, in many cases significant anisotropy of emanating signals can be attributed to a combination of shear dilatant forces and the effects of joint sets or existing fractures in the media. In this work the two-dimensional discrete-particle models DIBS and DIBSR are used to simulate the response of close packed polygonal blocks to rapid loading on the inside of circular and square openings.

NUMERICAL MODELS

Simulation calculations for this study were performed with the Discrete Interacting Block System (DIBS) numerical model[5,6] and a new *rounded corner* version of that model, DIBSR. The DIBS model, which is similar to earlier "distinct-element" models[7], calculates the motion of each discrete polygonal block as it responds to contact forces, boundary and applied loads and gravity. Arbitrary (convex) polygonal shapes are allowed for each particle or block. Several simplifying assumptions make the calculations tractable. The particles themselves are assumed to be rigid (*i.e.*, non-deformable); only the contacts deform. Such an assumption is quite appropriate when dealing with hard, jointed rocks. All contacts between polygons are assumed to be *corner-on-side* (*i.e.*, temporary, sliding joint-elements or *contacts* are set-up at polygonal vertices, as needed). Small but finite "overlaps" occur as normal forces are developed. Similarly a finite, partially recoverable shear-strain develops in the contact before frictional sliding is initiated. In the rounded-corner version of the model *corner-corner* contacts are also allowed, and they serve to allow a smooth transition in the direction of the contact normal as a contact moves from one side onto the next. Appendix A briefly describes the contact detection algorithms and integration equations used in DIBS and DIBSR.

CONTACT FORCES

Contact forces are inherently dissipative. The energy losses are due to a variety of factors including plastic deformation in the contact region, breaking of asperities, and frictional sliding. Various force models are available in DIBS to account for such loses; most involve position dependent hysteresis for cyclic force displacement paths. In addition, a small viscous (*i.e.*, linear, velocity-dependent) term can be added to the normal-direction contact force to aid in damping out high frequency oscillations.

Normal Force Models

The calculations in this study utilized two different normal force models, one that approximates the behavior of contacts between elastic-plastic spheres, and one that approximates joint-closures for rocks.

Inelastic Linear Model. Hertz's solution[8] for the normal force between contacting elastic spheres (or spherical asperities) gives a normal force that increases as the 3/2 power of the relative approach (or "overlap") of the spheres. On the other hand, measurements of force displacement paths during dynamic impacts of metal spheres[9] and finite element calculations of force-displacement behavior for impacting elastic-perfectly-plastic spheres exhibit an almost linear loading, combined with a steeper and nearly linear unloading.[10] This inelastic behavior, representing energy lost to plastic deformation, is modeled in DIBS (after Ref 10) as a linear loading curve, with a slope K_1, and a steeper linear unloading slope, K_2. The normal force, F_n, is given by,

$$F_n = \begin{cases} K_1\alpha & \text{for loading, and} \\ K_2(\alpha - \alpha_0) & \text{for unloading.} \end{cases} \qquad (1)$$

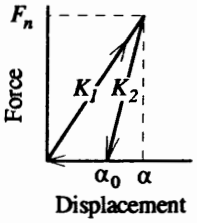

Fig 1

Unloading follows this steeper slope until the normal force is zero (with a finite "overlap," α_0, remaining). Upon further unloading the force remains at zero, or, upon reloading, it increases with slope K_2 until the original loading curve (K_1) is reached, (see Fig. 1). The slope of the unloading/reloading curve, K_2, can be set to increase linearly with the maximum force reached during a contact, or it can be set to a constant value, as was done in this study.

Nonlinear Rock-Joint Model. The combined effects of an initially soft, inelastic joint and the approximate deformation of a stiff elastic block are modeled in DIBS with a loading curve that has a monotonically increasing slope. The stiffness asymptotically approaches a value equivalent to the elastic response of intact rock at high loads.[11] The total deformation of both the block and the joint is assigned to the interface alone, in the model. Thus, the apparent overlap between two blocks in the model, includes the displacement associated with the actual deformation of the block. If d is the distance between the centroids of two contacting blocks, and E_r is the modulus of the blocks, an equivalent spring stiffness, K_r, can be defined between the centroids, $K_r = E_r ht/d$, where h is the block height and t is the thickness (see Fig. 2a). The model combines this "rock stiffness" with a contact relation for joints that has a vertical asymptote at a maximum joint closure, α_c. A commonly used form for such joint behavior[12,13] requires just two input parameters: the maximum joint closure, α_c, and the initial normal joint stiffness, K_1. The force displacement relation assumed for the joint is, $F = (K_1\alpha_c\alpha_j)/(\alpha_c - \alpha_j)$, where α_j is the displacement (*i.e.*, closure) of the joint. The rock is assumed to be *linear-elastic* with a force displacement relation $F = K_r\alpha_r$, where α_r is the displacement associated with the rock deformation. Rearranging these expressions we obtain,

$$\alpha_j = \frac{F\,\alpha_c}{F + K_1\alpha_c} \qquad \text{and} \qquad \alpha_r = \frac{F}{K_r} \qquad (2)$$

for the displacements of the joint and rock, respectively. The total displacement, α, is simply the sum of these two terms,

$$\alpha = \alpha_j + \alpha_r = \frac{F\,\alpha_c}{F + K_1\alpha_c} + \frac{F}{K_r} \qquad (3)$$

Equation (3) may be solved for F in terms of α, (4)

$$F = \frac{1}{2}[\alpha K_r - \alpha_c(K_1+K_r)] + \frac{1}{2}\left\{[(K_1+K_r)\,\alpha_c - \alpha K_r]^2 + 4K_1K_r\,\alpha_c\alpha\right\}^{\frac{1}{2}}$$

The slope of this force displacement curve, $dF/d\alpha$, approaches K_r as α approaches infinity,

$$\frac{dF}{d\alpha} = \frac{K_r}{2} + \frac{\alpha K_r^2 - \alpha_c K_r(K_r - K_1)}{2\left[\alpha^2K_r^2 - 2\alpha\alpha_c K_r(K_r - K_1) + (K_r + K_1)^2\alpha_c^2\right]^{1/2}} \qquad (5)$$

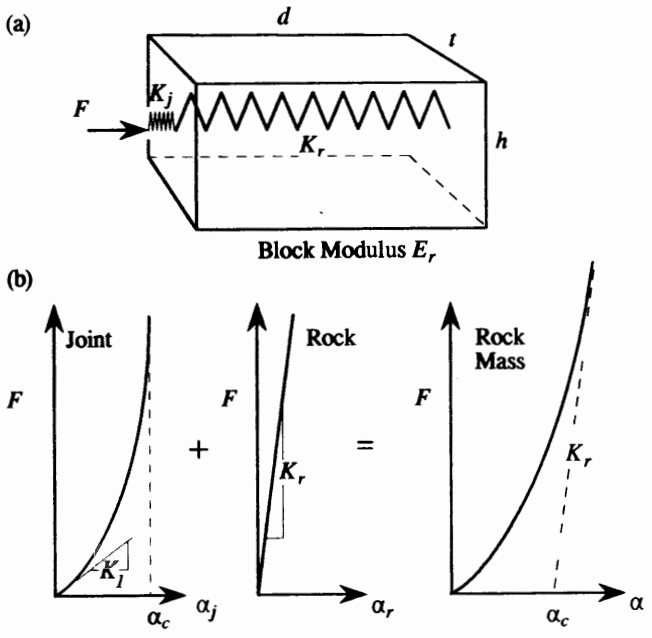

Fig 2(a) Schematic of and (b) Force-displacement curves for components of rock joint model.

Figure 2(a) is a schematic representation of the rock-joint model and Fig. 2(b) shows the qualitative behavior of the component and combined force-displacement curves. Various assumptions are possible for unloading and reloading with this nonlinear rock-joint model: (a) The unload and reload slopes are equal to K_r, (b) the unload and reload slopes are equal to the tangent of the loading curve at the point of initial unloading, and (c) Unload and reload slopes are set to a fixed (input) multiplier of the tangent slope at initial unloading. The selection of the unloading model determines the degree of energy loss during collisions.[11]

Tangential Friction Force Model

The tangential force model in DIBS is patterned after theoretical models for the friction forces acting between elastic spheres in contact.[14,15] In this theory the effective tangential stiffness of a contact decreases with tangential displacement until it is effectively zero when full sliding occurs. The effective tangential stiffness in the DIBS model, K_t, decreases in a similar manner;

$$K_t = \left\{ \begin{array}{ll} K_0\left[1 - \dfrac{T - T^*}{\mu F_n - T^*}\right]^{\gamma} & \text{for } T \text{ increasing} \\ K_0\left[1 - \dfrac{T^* - T}{\mu F_n - T^*}\right]^{\gamma} & \text{for } T \text{ decreasing} \end{array} \right\} \quad (6)$$

where, T is the total tangential force, K_0 is the initial tangential stiffness (usually set to a fixed fraction of the instantaneous normal direction stiffness), and μ is the coefficient of friction, γ is a fixed parameter usually set to 1/3 to agree with Mindlin's theory, and T^*, which is initially zero, is subsequently set to the value of the total tangential force, T, whenever the relative tangential slip reverses direction. If the normal force, F_n, changes during the contact, the value of T^* in the above expressions is scaled in proportion to the change in normal force.

On each explicit time step of the finite difference calculations a new tangential force, T', is calculated incrementally from the old value of the tangential force, T, the effective tangential stiffness, K_t, and the amount of relative surface displacement for the contact during the timestep, Δs, by the expression

$$T' = T + K_t \Delta s \quad (7)$$

with K_t given by Eqn. (6).

Figure 3 shows the tangential force *vs.* displacement as generated by Eqns. (6) and (7) for a series of ever increasing amplitude oscillations of the relative tangential surface displacement, s, with a constant normal force and an exponent $\gamma = 1/3$. This is not an exact fit to Mindlin's theory, however it is close for most loading paths and it is much simpler to calculate than some other approaches that have been attempted.[16] If the input parameter γ is set to a value larger than 1/3 (like 1.0), then the model has an even stronger hysteresis and the tangential force-displacement curve approximates the behavior observed for rough surfaces in contact[17] and the buildup to full sliding for flat metal surfaces.[18]

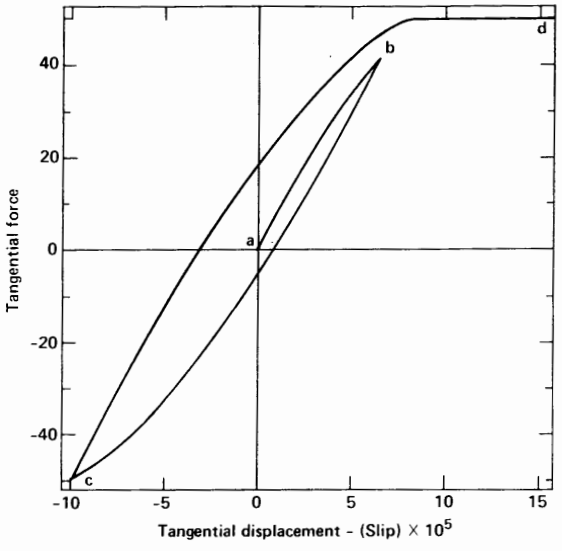

Fig. 3 Tangential force generated by incrementally slipping friction model.[10]

Time Integration

On each explicit time step of the calculation a loop through all contacts is performed once, accumulating the total force and moment on each particle for that configuration. Then, the equations-of-motion are integrated one time step and the time advanced. Each coordinate of each particle's position (*i.e.*, x, y, and θ) is integrated in time using a second order accurate scheme valid with non-uniform time steps. The x-coordinate of the centroid of a particle at time step $n+1$ is determined explicitly, for example, from the positions at steps n and $n-1$ and the x-direction force at the nth time step, F_x^n, by the expression: (8)

$$x^{n+1} = \left(1 + \frac{\Delta t'}{\Delta t}\right) x^n - \left(\frac{\Delta t'}{\Delta t}\right) x^{n-1} + \frac{1}{2}\left(\Delta t' \Delta t + \Delta t'^2\right) \ddot{x}^n \cdots + O\left(\Delta t^3\right)$$

where $\Delta t'$ is the time interval from n to $n+1$, Δt is the time interval from $n-1$ to n, and $\ddot{x}^n = F_x^n/m$, where m is the mass of the block. If the time step is uniform (*i.e.*, $\Delta t' = \Delta t$), and there are no velocity dependent forces, this expression reduces to the familiar, time centered, third order accurate Verlet scheme commonly used in molecular dynamics calculations.[19] Similar expressions are used for the y- and θ-coordinate integrations, based on the total y-direction force and the total moment acting on each block.

Because this is an explicit integration scheme, the time step must be kept below a stabililty limit determined by the stiffest spring and/or the smallest mass in the system. For accuracy the timestep must usually be kept significantly smaller than the stability limit. Empirical tests of accuracy have determined that on the order of 50 to 100 time steps per physical oscillation cycle are needed for the numerically integrated results to compare favorably with analytic solutions for simple multi-block systems (*i.e.*, ±1%).

SIMULATION CALCULATIONS

Close packed beds of randomly fractured rock are simulated as an array of Voronoi polygons.[20] These Voronoi cells are constructed about generating points that are initially arranged in a nearly regular array. Then, each layer, and each point in the layers, are randomly perturbed a small amount, so that the resulting polygons will have arbitrary convex shapes, with a relatively narrow size distribution and a narrow range of aspect ratios. Close packed sedimentary rocks, or other rocks with nearly orthogonal and nearly regular joint sets, are simulated as an array of nearly-horizontal through-running fractures or joints. Each layer is cut by a series of randomly spaced, nearly transverse, joints. The resulting bed consists of layers of close packed (nearly rectangular) trapezoidal blocks, with through-running joints in one direction (e.g., horizontal) and without any through-running joints in the transverse (e.g., vertical) direction.

Simulations where initial lithostatic loading may be important are usually "settled" under gravity loading before applying dynamic driving forces. A description of non-reflecting "silent" boundaries, "settling" procedures to rapidly approach static equilibrium, and various energy loss models is included in Ref. 11.

Shear Dilatancy Effects

Large Flat "Lift." Figure 4 shows successive snapshots of positions and velocities from a DIBS simulation wherein a large piston-like block is moved upward into a bed of close packed polygonal particles.[2] As shearing develops in the wedge shaped zones extending up and out from the large moving block, dilatation effects tend to "pinch" the central region, causing a noticeable turning of the velocity vectors towards the center. The reaction forces, outside the upward moving wedge, push down and out, causing the retaining blocks on the sides of the close packed region to move laterally. The dilatancy is a transitory phenomenon and, in this case, causes a single horizontal compressive pulse to be sent into the surrounding material.

Similar horizontal signals have been observed during explosive "lifting" of large rock masses while making retort beds for *in situ* recovery of shale oil. These signals were delayed in time from the initial outgoing compressive wave emanating directly from the explosive charge, leading to the conclusion that they were a response to the motion of the overburden material.[2]

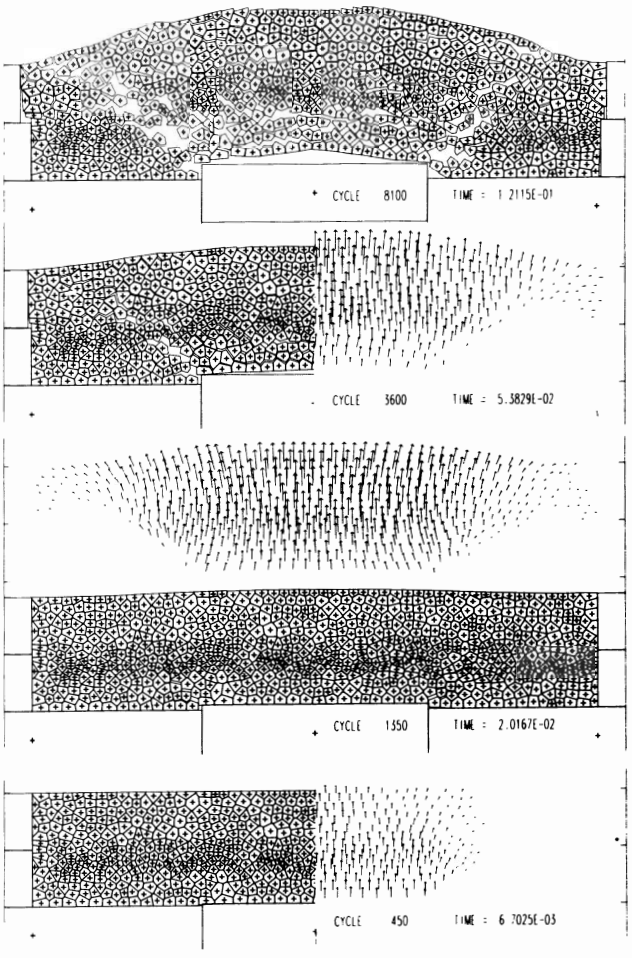

Fig. 4 Position and velocity plots showing dilatancy induced "pinch" effect.

Explosive Cratering. The potential significance of strong shear-dilatant forces for non-contained explosions in fragmented rock is also evident in Fig. 5 showing two snapshots of a DIBS cratering simulation. The first frame shows the close packed set of polygonal blocks representing a fractured rock, shortly after an initial impulse has been applied to the blocks surrounding a cavity. The velocity vectors are initially pointing radially outward from the simulated shot point. The second frame shows the subsequent positions and velocity vectors after the overburden material has separated from the lower "crater" surface. Note that the velocity vectors of the throwout material are primarily vertical at this point—a result of the temporary large shear-dilatant forces that existed as the overburden material displaced relative to the lower stationary material.

The geometry and driving forces in this simulation were chosen to simulate a nuclear cratering event, SULKY[21], conducted at the Nevada Test Site in the mid-1960's. In this event a nuclear device with a yield of 90 tons (equivalent TNT) was detonated at a depth of 27.4 m in dry basalt. The rock had pre-existing joint sets resulting in a

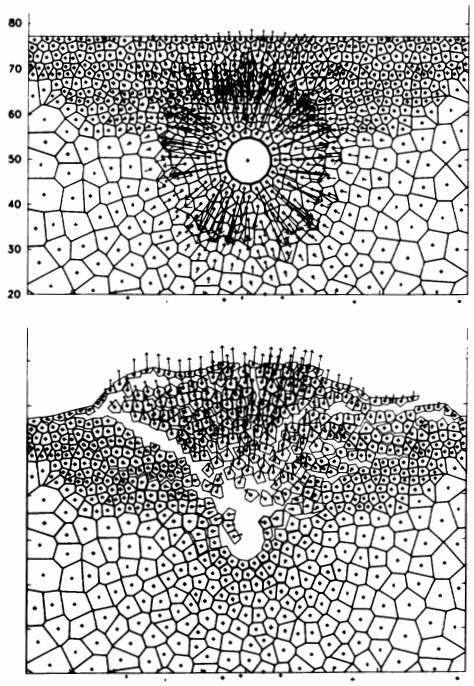

Fig. 5 DIBS simulation of explosive cratering in fragmented rock showing nearly vertical throwout debris velocities resulting from shear dilatancy effects.

distinctly blocky geology. The duration of the cavity loading in the simulation was tailored to be similar to cavity pressures calculated in hydrocode simulations of the explosion. The amplitude of the 2-dimensional cavity loading in the DIBS simulation was adjusted to make the simulated free surface velocity match the measured field value of 26 m/s. Examination of high speed motion pictures of the field event revealed that the throwout material moved primarily straight up with only a small radial velocity. Most of the throwout material fell back into the temporary crater, creating a post shot mound. The DIBS simulation produced similar behavior, including a comparable amount of bulking of the throwout material.

Viscous Damping Effects. In the first frame of Fig. 5 the initial signal has already reached the free surface and careful examination of the velocities of blocks, in what will subsequently become a shear zone, shows that deviation from radial motion is already occurring. This calculation was run with a version of DIBS that had velocity dependent viscous damping as the only normal-direction energy loss mechanism acting at the contacts.[5] This linear dashpot model produced extremely high forces under rapid dynamic loading (and correspondingly high, and velocity-dependent, propagation velocities through the simulated medium). This rapid wave speed allowed the material surrounding the loaded cavity to "know" about the boundaries and the free surface even during the first few milliseconds of the simulated explosive loading. This viscous "precursor" allowed blocks 20 meters below the simulated free surface to begin to respond to its effects within two milliseconds after loading began.

The subsequent large-amplitude main wave, traveling at a slower speed, also reflected from the free surface, producing significant displacements along the shearing planes (at approximately 45 degree angles up on each side of the cavity). The resulting shear displacements caused the dilatant force effects as evidenced by the altered direction of the throwout debris; however, the existence of the small, rapid, precursor produced by the viscous damping, prompted the authors to utilize more realistic force models in subsequent dynamic simulations.

Anisotropic Wave Propagation

Symmetric Waves Through Voronoi Array. In the SULKY simulation above, the initial outgoing compressive wave spread isotropically from the circular cavity source region. The wave propagation velocity for a two-dimensional spring-mass network is given by the expression, $c = \Delta l\sqrt{(K/m)}$, where Δl is the distance between centers, K is the effective spring constant between mass centers in the direction of propagation, and m is the mass associated with each centroid. It is perhaps worth noting that this wave speed is expected to be independent of the particle size (for two-dimensional systems) as long as all particles have the same areal density and have an aspect ratio of one. Thus, the upper and lower regions of the grid in Fig. 5, which have different average block sizes, should have roughly the same propagation velocity.

In at least an approximate way, the simulation shown verifies this expectation. Further simulations, of more deeply buried explosives, confirm that out-going waves propagating through a close packed array of nearly uniform size Voronoi polygons (connected by springs at their vertices) spread out isotropically from an initially circular pressurized cavity. Redirection, or anisotropy in the particle velocity vectors occurs later in the SULKY simulation, only because relief waves, reflected from the free surface, allow shearing displacements to develop. These shearing motions, in turn induce dilatancy and the resultant forces affecting particle motions.

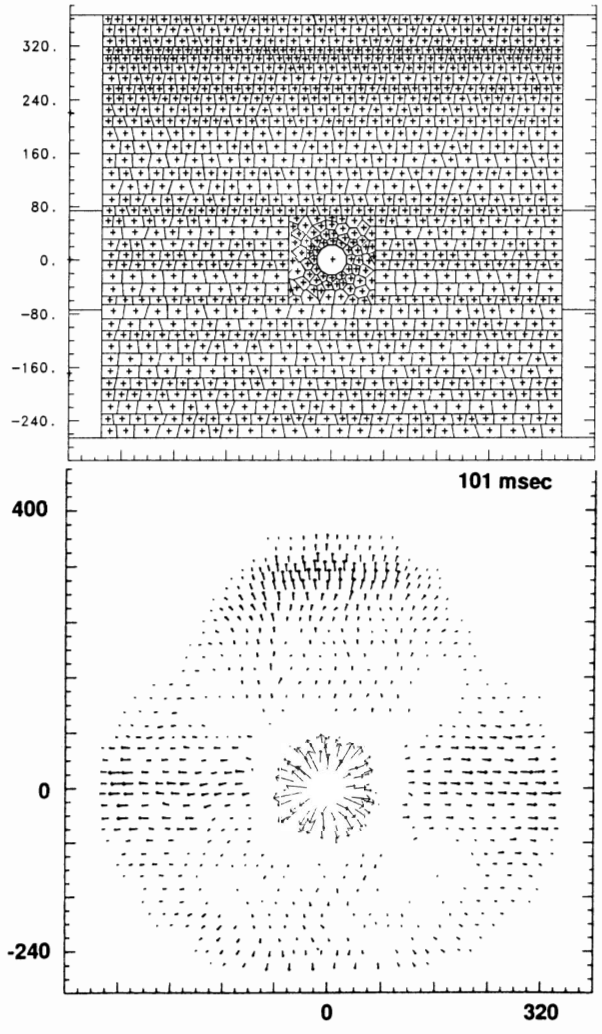

Fig. 6 (a) Layered geology surrounding random Voronoi region around rapidly loaded cavity, (b) velocity vectors at 0.017s and 0.101s.

Anisotropic Waves in Near-Orthogonal Joint Sets. or The Impossibility of Diagonal Propagation. Figure 6(a) shows another close packed set of polygonal particles surrounding a circular cavity to which a short duration loading pulse is applied. The region immediately around the pressurized cavity is filled with Voronoi polygons. At approximately three cavity radii from the center, the Voronoi polygons abruptly end and a nearly regular close packed set of almost brick-like trapezoids is encountered. This brick-like structure, with predominantly horizontal and near-vertical interfaces, creates a strong directionality in the way energy emanates from the near-cavity region.

The velocity vector plot in Fig. 6(b) is an overlay of velocity vectors from two different times. The inner array of nearly radial arrows, is a picture of the velocity vectors at a time 17 ms after the start of loading. The outer set of arrows, pointing predominantly in the horizontal and vertical directions, is the set of velocity vectors at 101 ms after the start of loading (The actual loading history lasted beyond 101ms, but the amplitude decreased rapidly after the first 10 ms, so that the residual load primarily served to prevent a strong rebound back into the cavity). The initial, nearly symmetric, picture occurs at a time when the outgoing wave is still completely within the Voronoi polygon region. As the wave propagates beyond this region, into the brick-like region, strong directionality develops with almost no energy propagating diagonal to the predominant joint sets. This calculation was run with the corner-on-side DIBS model, using the nonlinear rock-joint model with a coefficient of friction at contacts of $\mu = 0.7$.

Figure 7(a) shows an array of trapezoidal blocks dipping 30 deg down on the left. A square cavity (or tunnel) is placed near the middle of the dipping bed. The rounded-corner version of the model, DIBSR, was used to simulate rapid loading of the interior of the cavity or tunnel. Unlike the previous simulations, no initial lithostatic loads were applied to this bed, and gravity was not acting. The inelastic-linear model was used with $K_2 = 4K_1$, and the coefficient of friction $\mu = 0.5$. To simulate an explosion-like situation, a loading pulse of constant magnitude and 2 ms duration, followed by a rapid decrease in load was applied to each of the blocks on the flat faces of the oppening. Horizontal loads were applied, in the positive and negative x-direction, to the blocks comprising the right and left faces of the tunnel, respectively. Positive and negative vertical loads were also applied to the blocks comprising the top and bottom of the tunnel, respectively. No loads were applied directly to the corner blocks.

Figure 7(b) shows the velocity vectors during the peak loading of the interior blocks (*i.e.*, at 2 ms after the start of the problem). Most of the early motion is in the horizontal and vertical directions, in response to the high applied loads. Figure 7(c) shows the velocity vectors around the tunnel at a time of 10 ms, when the applied loads on the interior have been reduced by two orders of magnitude from their earlier high values. The most stiking feature to note in this figure is the alignment of the velocity vectors with the dipping joints and perpendicular to the dipping set. The finite width pulses that initially were traveling in either the horizontal or vertical directions appear to have been bifurcated into waves traveling parallel or perpendicular to the bedding planes. By the time the initially horizontal signal has traveled a distance of a few cavity diameters it has all but disappeared, and only the parallel and perpendicular waves remain.

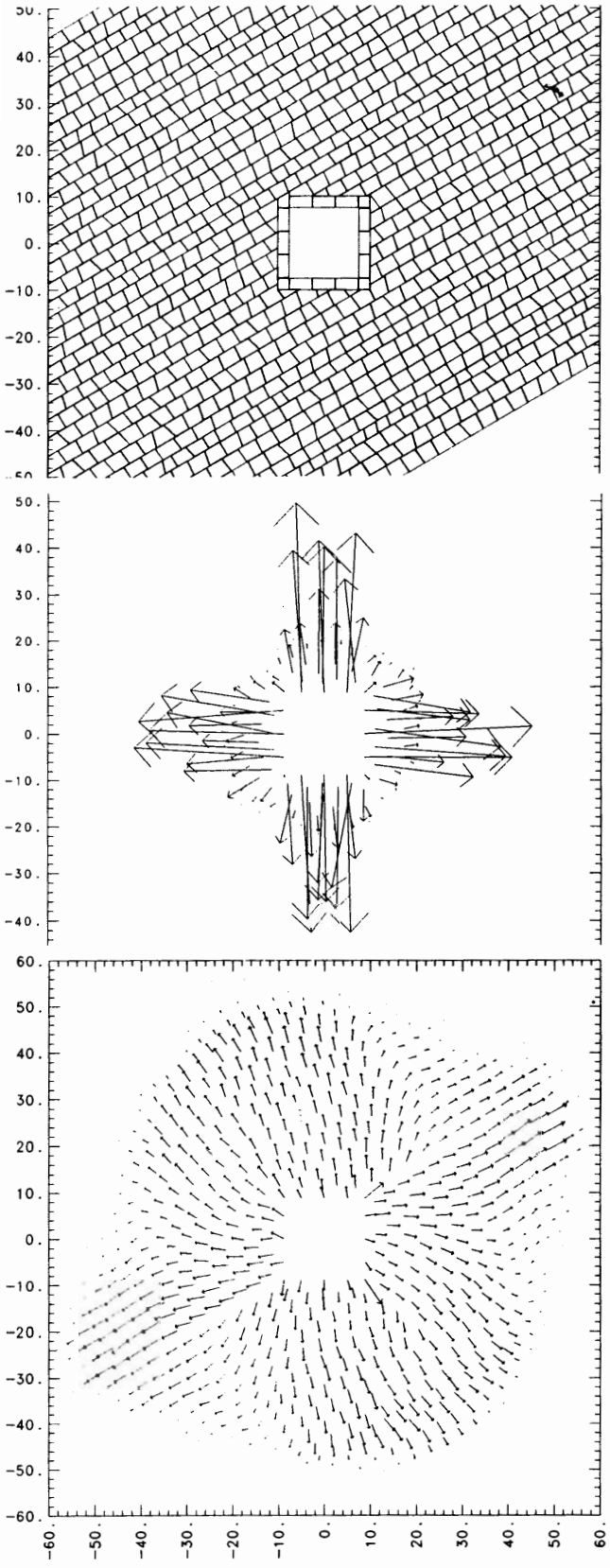

Fig. 7 (a) Layered geology dipping at 30 deg., (b) Velocity vectors during horizontal and vertical loading of square opening, (c) Velocity vectors after propagating 3 cavity diameters.

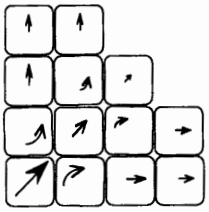

Fig. 8

Figure 8 can be used to illustrate, schematically, how this bifurcation can occur. The lower left block is moved into a regular set of square blocks (with rounded corners). If there were no friction acting between blocks then no shear forces could be transmitted across contacts. In such a situation, the two blocks first touching the moving block would move off in directions perpendicular to the surfaces of contact. In other words, bifurcation would be immediate and complete. Only the two outer rows of blocks would move, until the driven block moves far enough to contact the corner of the block directly in its path (at which time most of its momentum would probably already have been transferred to the other blocks).

To the extent that tangential frictional forces are usually less than normal forces (*i.e.*, coefficients of friction are usually less than one), we might expect to see a tendency for real frictional contact response to include some aspects of the hypothetical frictionless case. In addition, with real frictional contacts, the two initially contacted blocks would have both horizontal and vertical velocity components, as well as rotational responses to the frictional forces from the driven block. The rotational motion requires dilatation of the close packed assembly. Thus, reaction forces develop resisting the rotation, but pushing out on blocks surrounding the block attempting to rotate. This will add to the horizontal and vertical forces transmitted to the next layer of blocks.

The case illustrated with Fig. 8 exaggerates the actual bifurcation from a finite width pulse since the initial wave in the illustration is only one block wide. However, the edges of any finite width wave attempting to propagate diagonally through a regularly jointed set of blocks will experience phenomena similar to those illustrated.

CONCLUDING REMARKS

The simulation calculations presented in this paper illustrate the importance of considering the discrete joint sets and geological structure when dealing with waves in hard rock. Regular, nearly orthogonal, joint sets make a material inherently anisotropic. These calculations indicate that the anisotropic effects in such materials may be so profound as to all but prevent propagation of finite dimension pulses in directions diagonal to the predominant joint sets.

When significant displacements occur in initially close packed configurations (such as jointed or fragmented rocks), the resulting shear dilatant forces can dramatically change the direction of particle velocities (pushing them away from the shearing plane). This type of behavior can contribute to such observable effects as secondary seismic sources from large buried explosions, and shifting of the direction of throwout debris to nearly vertical trajectories in slightly over buried cratering blasts in hard rock.

It is hoped that these calculations, and the insight gained from them, will serve to demonstrate the need to consider the discrete nature of, especially, geologic materials when making predictions of response to dynamic loadings. Most continuum calculations made with finite element or finite diference "hydrocodes" do not employ anisotropic material models or shear dilatancy models. Without including these very real effects, such calculations may have significant difficulty predicting even the *qualitative* response of jointed media.

ACKNOWLEDGEMENTS

This work was partially funded by the Treaty Verification Program, the Military Applications Program, the Institutional Research and Development Program and the Fossil Energy Program of Lawrence Livermore National Laboratory, under contract W-7405-ENG-48 with the U.S. Department of Energy, and with funding from the U.S. Defense Nuclear Agency. The authors would like to thank R. Shaffer S. Taylor and H. Patton for useful discussions during the course of this work.

REFERENCES

[1] Chappell, B.A."Deformational Response in Discontinua," *Int. J. Rock Mech. Min. Sci. & Geomech. Abstr.*, **16**, 377-390 (1979), and "Load Distribution and Redistribution in Discontinua," *ibid.* p391-399

[2] Britton, K. and O.R.Walton, "Brittle Fracture Phenomena - An Hypothesis," in *Proceedings 2nd Int'l. Symp. on Rock Fragmentation by Blasting*, Keystone, CO Aug 23-28, 1987.

[3] Butkovich, T.R., O.R. Walton and F.E. Heuzé, "Insights in Cratering Phenomenology Provided by Discrete Element Modeling," *Key Questions in Rock Mechanics: Proc. 29th US Symposium*, P.A. Cundall, R.L. Sterling & A.M. Starfield, eds., A.A. Balkema, Rotterdam, (1988) pp. 359-368.

[4] Britton, K., Private communication (1987)

[5] Walton, O.R., "Explicit Particle Dynamics Model for Granular Materials," *Numerical Methods in Geomechanics, Edmonton 1982*, Z. Eisenstein, ed., A.A. Balkema, Rotterdam, pp. 1261-1268.

[6] Walton, O.R., *Particle Dynamics Modeling of Geological Materials*, Lawrence Livermore National Lab. Rept. UCRL-52915, 1980 (avail. from University Microfilms, Ann Arbor, Mich.).

[7] Cundall, P.A., *Rational Design of Tunnel Supports: A Computer Model for rock Mass behavior Using Interactive Graphics for the Input and Output of Geometric Data*, US Army Corps of Engineers, Technical Report MRD-2-74, (1974).

[8] Timoshenko, S. and J.N. Goodier, Theory of Elasticity, 2nd ed., McGraw Hill, NY, 1951.

[9] Goldsmith, W., *Impact*, Edward Arnold Pub., London, 1960.

[10] Walton, O.R. and R.L. Braun, "Viscosity, Granular-Temperature, and Stress Calculations for Shearing Assemblies of Inelastic, Frictional Disks," *J. Rheology*, **30** (5), 949-980 (1986).

[11] Heuzé, F.E., O.R. Walton, D.M. Maddix, R.J. Shaffer and T.R. Butkovich, "Analysis of Explosions in Hard Rocks: the Power of Discrete Element Modeling," proceedings of Int'l Conf. Mechanics of Jointed and Faulted Rocks, Vienna, Austria, April 18-20, 1990.

[12] Goodman, R.E., *Methods of Geological Engineering*, West Publishing, NY, 472 p., 1976.

[13] Bandis, S.C., A.C. Lumsden and N.R. Barton, "Fundamentals of Rock Joint Deformation," *Int. J. Rock Mech. Mining Sci.*, **20** (6), pp 249-268, (1983).

[14] Mindlin, R.D., *J. Appl. Mech.Trans. ASME*, **16**, 259 (1949).

[15] Mindlin, R.D. and H. Deresiewicz, *J. Appl. Mech.Trans. ASME*, **20**, 327 (1953).

[16] Patrakis, E. and R. Dobry, "Micromechanical Behavior and Modeling of Granular Soil," Rept. to US Air Force under grant No. AFOSR-86-0135, Rensselear Polytechnic Inst., Troy, NY (1989).

[17] Mullier, M., U. Tüzün and O.R. Walton, "Micro-Mechanical Modeling of Load Dependent Friction in Contacts of Elastic Spheres," *Powder Technology* (in press, 1991).

[18] Oden, J.T. and J.A.C. Martins,in *Computer Methods in Appl. Mech. and Engng.*, North Holland, Amsterdam, 1984.

[19] Allen, M.P., and D.J. Tildesley, *Computer Simulation of Liquids*, Clarendon Press, Oxford, (1987).

[20] A Voronoi polygon is that unique region of space closer to the generating center than to any other generating point in space.

[21] Lutton, R.J., and Girucky, F.E. "Project SULKY: Geologic and Engineering Properties Investigations," U.S. Army Corps of Engineers, Vicksburg, Mississippi, Report **PNE-720**, Nov. (1966).

[22] Alder, B.J., and T.E. Wainwright, "Studies in Molecular Dynamics. I. General Method," *J. Chem. Phys.*, **31**, 3, (1959).

[23] Cundall, P.A., *UDEC - A Generalized Distinct Element Program for Modeling Jointed Rock*, technical report to U.S. Army under contract No. DAJA37-79-C-0548, Peter Cundall Associates, 1980.

[24] Cundall, P.A. and R.D. Hart, *Development of Generalized 2-D and 3-D Distinct Element Programs for Modeling Jointed Rock*, Technical Report, Itasca Consulting Group, Minneapolis, MN, 1983.

APPENDIX A
Contact Detection and Searching Algorithms

Contact Geometry

Any corner of any polygon is allowed to contact any side of any other polygon. Automatic, efficient, contact search and detection algorithms are essential for the calculations to proceed without undue computational expense. A variety of methods to improve the efficiency of detecting particle contacts or collisions have been developed over the years[19] since Alder and Wainwright first described the general method of molecular dynamics.[22] The detection of contacts is done using a nested geometric search algorithm, with the complexity of the testing increasing as the search level approaches the actual determination of whether an individual corner of one polygon is contacting a specific side of another. On the largest scale, the calculational space is divided into a regular grid of rectangular zones or *boxes*. A particle is assigned to a box if its *range* intersects the box. The *range* of a particle is the space contained in a square with sidelength $2\varepsilon_s$ longer than the diameter of the smallest circle (centered at the particle's centroid) that circumscribes the particle, where ε_s is a search distance for potential new contacts, (see Fig. A1).

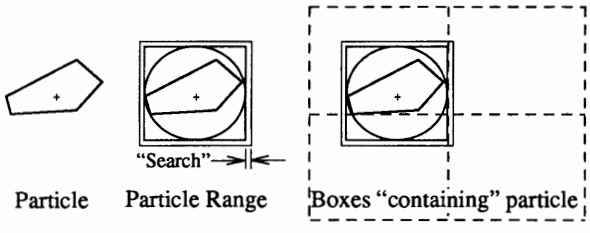

Fig. A1 Assignment of one particle to four *boxes* intersecting its *range*.

Particles assigned to the same box are tested to see if their *ranges* overlap. If they do, then more detailed testing is performed. For convex particles only the vertices on the side "nearest" the other particle need to be examined for possible contact. The selection of only the vertices on the "nearest" side of each particle is accomplished by examining cross products of the vector joining the centers of the two particles with vectors from the centroid of one particle to each vertex of the other polygon. The maximum and minimum cross products correspond with the first and last vertices used in a final search for contacts.

Figure A2 shows two convex polygons, I and J, and the maximum and minimum angles as viewed from each block centroid. In this figure, vertex 8 (of polygon I) is the minimum, and vertex 3 is at the maximum angle. Only vertices between 8 and 3 (*i.e.*, members of the set {8,9,1,2,3}) are considered as possible contacting corners. Similarly only vertices in the set {5,6,1,2} of block J are considered as possible contacting corners. The algorithm that tests for contacts starts with vertex 3 of block I and the side between vertices 5 and 6 of block J. First a test is made (*i.e.*, the sign of a cross product is checked) to determine if vertex 3 is in *sector* 5-6. If the vertex is not in the sector then the sector number is incremented and, in this case, vertex 3 would be checked to see if it is in sector 6-1 of block J. If the vertex is in the sector its distance to the side [y_t in Eqn (A1) below] is checked. A *contact* is established and appropriate indices put into a linked list of contacting neighbors if the vertex is within the search distance, ε_s. If the vertex is not close enough to be considered a potential contact then the vertex number is decremented and the next vertex tested. The algorithm steps sequentially through the vertices and sides of each polygon, going clockwise around one and counter clockwise around the other, without ever backing up. Once the near-neighbor or *contact lists* are established the forces are calculated according to the procedures described in the text of the paper.

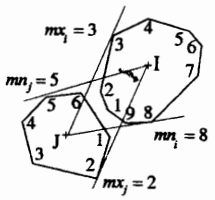

Fig. A2

Corner-Side Contacts

Figure A3 illustrates the geometry of a typical DIBS contact between corner C of Block J and side $\overline{AB}$ of Block I. The corner A of block I acts as the origin for a rotated local coordinate system wherein x_t is the distance along the side AB to where the contacting corner, C, is located, and y_t is the transformed perpendicular distance from corner C to the line $\overline{AB}$. The "overlap," α is defined to be the negative of y_t.

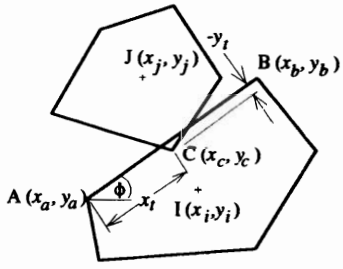

Fig. A3 Schematic of *corner on side* contact in DIBS

The normal and shear forces at each contact are determined in terms of the local transformed coordinates x_t and y_t given by:

$$x_t = (x_c - x_a)\cos\phi + (y_c - y_a)\sin\phi \qquad \text{(A1)}$$

$$y_t = (y_c - y_a)\cos\phi - (x_c - x_a)\sin\phi \qquad \text{(A2)}$$

For efficiency, the inverse of the side length of each edge of each polygon is calculated only once, as the geometry for each block is defined. Subsequently, this value is used to determine the sine and cosine values in Eqns. (A1) and (A2) without any square roots, trigonometric function calls or divides.

For normal-force calculations, the overlap, $\alpha = -y_t$, determined from Eq. (A2), is used in Eqns. (1) or (6). For tangential force calculations, the relative surface displacement, Δs, is obtained from the change in x_t from one time step to the next. Whenever a corner is beyond the end of a side (*i.e.*, $x_t < 0$, or $x_t >$ the side length) the force for that contact is set to zero. "Cemented" or tension-bearing contacts are allowed in the DIBS model but, for all of the calculations described in this paper, only frictional, repulsive contacts were used. For these frictional contacts, whenever y_t is positive (*i.e.*, the blocks are not touching) the contact forces are set to zero.

Rounded-Corner Contacts

The rounded corner version of the model, DIBSR, builds on the original DIBS construct, wherever possible. From a users point of view the model functions almost the same as the sharp corner version. Internally, however, there are some significant differences. Input geometric data for each block contains the coordinates of an "outer" polygon with sharp corners (this is just the ploygon the DIBS model would use). When the problem is initialized (*i.e.*, as geometric data is stored) a circle of fixed radius, r_c, is placed inside each vertex, tangent to the two adjacent sides. A new "inner" polygon is constructed connecting the centers of each of the corner circles. The side lengths of the inner polygon are exactly the same as the lengths of the line segments between tangent points on the outer polygon (see Fig. A4). The coordinates of the vertices of the inner polygon replace the original outer polygon coordinates in the computer storage arrays, and this inner polygon is used in all contact searching algorithms. Such a construct facilitates the use of most of the same searching algorithms for contact detection as were used in the original sharp corner version of the model. One major modification is that "overlap" is considered to occur when the two inner polygons are a distance apart equal to the sum of their respective corner radii. When a corner is contacting a side the transformed local coordinates, x_t and y_t, are still determined by Eqns. (A1) and (A2). The overlap, α, is now defined to be,

$$\alpha = r_i + r_j - y_t \ , \qquad \text{(A3)}$$

where r_i and r_j are the radii of the corners for blocks I and J, respectively (see Fig. A4).

This, in effect, moves the real surface (for determination of contact forces) a distance, r_c, outside the stored inner polygon .

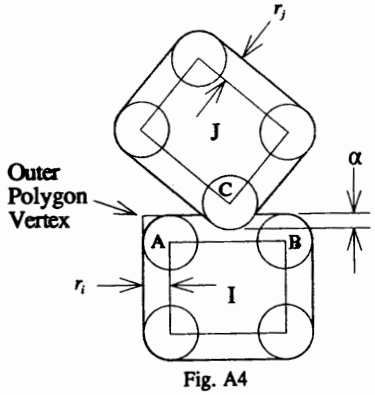

Fig. A4

The other major difference for the rounded corner model occurs when a contacting corner goes beyond either end of the "side"of the inner polygon, (i.e., $x_t < 0$, or $x_t >$ |AB|). When this occurs the contact is redefined to be a *corner-corner* contact.

The existing contact forces, including the current partially recoverable tangential shear strain, are unaffected by the transition form one contact type to another. Only the indices in the linked list of contacts, indicating which corner and/or side of which blocks comprise the contact, are affected. This contact information is in a separate, dynamic, linked list for each block . Each block's list contains the indices of the sides and/or corners of blocks contacted by that block.

For corner-corner contacts equations (A1) and (A2) are replaced by direct calculations of the relative overlap, α, and the relative slip Δs. If two corners, A and C are in contact, with **R** being the vector from corner A to corner C on the last time step (*i.e.*, from the "old" location of A to the "old" location of C), and **R'** is the vector from the current location of corner A to the current location of corner C, then the current overlap between the corners, α', is given by

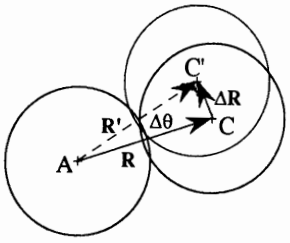

Fig. A5

$$\alpha' = (r_i + r_j) - \sqrt{R'^2_x + R'^2_y} \quad . \tag{A4}$$

The average value of this overlap during the last time step is approximately,

$$\bar{\alpha} = \frac{1}{2}(\alpha + \alpha') \tag{A5}$$

where α is the value of the overlap on the last time step. The change in relative angle between the the contacting corners, $\Delta\theta$, can be approximated by a series expansion for the arcsine,

$$\Delta\theta \approx \sin\Delta\theta \left(1 + \left(\sin^2\Delta\theta \left(\frac{1}{6} + \frac{3}{40}\sin^2\Delta\theta\right)\right)\right) + \cdots \tag{A4}$$

and, we can obtain $\sin\Delta\theta$ from the known magnitudes of **R** and **R'**,

$$\sin\Delta\theta = \frac{\mathbf{R}\times\mathbf{R}'}{|\mathbf{R}||\mathbf{R}'|} \quad , \qquad (\text{where} \quad R = r_i + r_j - \alpha\,).$$

The relative slip between the surfaces is, then, given by,

$$\Delta s = \left(r_j - \frac{\bar{\alpha}}{2}\right)(\Delta\theta_j - \Delta\theta) + \left(r_i - \frac{\bar{\alpha}}{2}\right)(\Delta\theta_i - \Delta\theta)$$

where $\Delta\theta_i$ and $\Delta\theta j$ are the changes in orientation angle (*i.e.*, the amount of rotation) during the last time step for blocks I and J respectively.

When corner-corner contacts occur, both corners involved, separately, detect, store, and calculate forces for the contact. This slight redundancy has two effects of significance. First, for close packed configurations of nearly equal size particles, there are an average of four contacts per block length acting between two successive rows (such as the rows in Fig. 6 in the text). The number of active (i.e., force generating) contacts is nearly independent of the allignment of the joints or blocks if one layer slides over another. The average number of contacts per unit length is needed to determine the joint stiffness for individual contacts that will produce a desired bulk elasticity (or wave propagation velocity) for the close packed assembly.

The second effect of having two "pieces" to the corner-corner contact forces, is that when two isolated blocks slide past one another the effective stiffness of the joint between them can vary (albeit smoothly) by as much as a factor of two.

The major advantage of the rounded corner approach is that it allows physically realistic frictional sliding along interfaces comprised of many blocks in contact. The sharp corner model could allow corners to unphysically "hang up" as a block attempted to slide onto the end of another block in the contacting row. Avoidance of such corner-corner "hang-up" was the major motivation for adding rounded corners to the DIBS model (as it was for Cundall in constructing the similar UDEC model.[23,24])